Appl. Phys. B 92, 431–438 (2008)
DOI: 10.1007/s00340-008-3131-2

Applied Physics B
Lasers and Optics

M. CIOFINI[1]
E. FAVILLA[1]
A. LAPUCCI[1]
E. SANI[1,✉]
A. CAPANNI[2]
L. TOMMASI[2]

MILD: a laser altimeter transmitter for a Mercury planetary orbiter

[1] CNR – INOA, Largo Enrico Fermi 6, 50125 Firenze, Italy
[2] Selex Galileo S.p.A., Space B.U., Via Albert Einstein, 35, 50013 Campi Bisenzio (Firenze), Italy

Received: 15 January 2008 / Revised version: 11 June 2008
Published online: 1 August 2008 •

ABSTRACT We report on the design and preliminary development of a micro laser (MILD) breadboard (BB). The laser source is designed to be used as the transmitter unit of a laser altimeter for planetary investigations. The reference scenario is the ESA BepiColombo mission to Mercury (presently scheduled to be launched in 2012) but possible applications to minor solar system bodies may be included.

In order to fulfil the laser source requirements for this kind of application we adopted a master-oscillator-power-amplifier (MOPA) scheme. Analysis of the MO efficiency, pulse duration and beam characterisation in different resonator configurations is described together with the preliminary PA performance on a $\pm$ 10 °C temperature range.

PACS 42.55.Xi; 42.60.By; 42.60.Da

1 Introduction

The laser source requirements for spacecraft altitude measurements are numerous and very demanding: low beam divergence ($M^2 < 1.5$), short (few-ns) high energy laser pulses with good energy and length stability. Moreover, due to the thermally harsh environment of the Mercury orbit with large excursions in spacecraft temperature expected, the key aspect of the laser design is insensitivity of laser performance to temperature variations. To cope with the requested laser characteristics, we choose a master-oscillator-power-amplifier (MOPA) scheme. In this way we decouple the output pulse energy characteristics, which are driven basically by the power amplifier (PA) stage from the mode selection and pulse forming steps, which are provided by the master oscillator (MO). The MO is a fibre-coupled end-pumped Nd:YAG rod, with a quasi-semi-confocal resonator. To achieve the required pulse stability the pulse generation is performed by means of a rubidium titanyl phosphate (RTP) active Q-switch. While to obtain the required amplification within a compact device we adopt a PA scheme based on a diode side-pumped multi-pass Nd:YAG slab amplifier. In this scheme the low-power input beam is propagated forth and back in the side-pumped slab by a two mirror system producing a 5-pass first amplification step, and then it is sent backwards into the slab, undergoing a second 5-pass zigzag path into the gain medium. The amplified beam leaves the active medium on the same side where the low-energy input beam enters, with a small angle with respect to it, and it is coupled out using this angular shift.

The main scope of this work is to characterize the output performance of the laser source on a 20 °C range of its operational temperature. To better understand the master oscillator and power amplifier behaviors, we have analyzed them separately.

2 Master oscillator performance

2.1 *MO design*

The MO pump system is based on a 100 W Qcw laser diode bar source coupled into a multimode fiber, with peak emission wavelength 808 $\pm$ 3 nm at 24 °C. The diode radiation emitted from the fiber end is then focused close to the end of the 15 mm long Nd:YAG rod by means of an optical system with magnification around 1. At the end of the focusing optics the pumping system delivers up to 130 mW in 200 μs pulses at 10 Hz repetition rate.

To achieve the required pulse length (5–8 ns) and pulse length stability ($\simeq$ 10% of the pulse length) we have to put particular care into the MO cavity design. Considering that the pulse duration variations are mainly due to longitudinal mode beating, a reduced pulse length variation translates into a high output coupler reflectivity. Indeed at high pumping levels the Q-switched pulse duration time gets close to the cavity decay time T_c. Since T_c is equal to the cavity round trip time T_{rt}, divided by the cavity loss factor Γ, a short pulse is obtained by choosing a short cavity. Moreover a short cavity is advantageous also because produces a larger free spectral range FSR, that means a higher longitudinal mode beating frequency. This improves the pulse length stability in the absence of an intracavity longitudinal mode selection element. In fact, an intracavity mode selector would increase the cavity losses and thus the pulse duration time.

Assuming a pulse duration time τ_P of the order of 1.5–2 cavity decay times, our pulse specifications translate into a cavity length $L \leq$ 12–15 cm. Efficiency extraction and cavity stability considerations led us to choose a resonator with a waist located close to the pumped side of the active medium.

✉ Fax: +39-55-2337755, E-mail: elisa.sani@inoa.it

With this choice we can easily obtain high above-threshold factors and thus shorter pulse durations. This leads us to the selection of a quasi-semi-confocal-resonator with the rear flat mirror defined by one end face of the rod. In particular our MO resonator has been designed in such a way as to minimize mode variation caused by changes in curvature and position of the optical components (due, for instance, to thermal lensing). For stability reasons we adopted dimensions close to the condition $g_1 g_2 = 1/2$ for the cavity g parameters [1]. This together with the quasi-semi-confocal resonator scheme ($g_1 = 1$) produces a $g_2 \simeq 0.5$ that is $R_2 \simeq 2L$. Since low g-parameter values produce a higher mode selectivity, our choice also gives acceptable mode discrimination. In our system with low duty cycle (200 µs pulse duration and 10 Hz PRF) and a maximum peak power of the order of 50 W on a pump spot size around 0.5 mm, we estimate from FEM calculations a pulsed lens with power $f_{\text{th}} > 10$ m. Our resonator design has been calculated in such a way as to withstand thermal lens effects with a ten times higher power.

2.2 *MO extraction efficiency and pulse duration: experimental results*

As detailed in the previous section, the development activity of the master oscillator was driven by the requirement of efficient extraction of short (few-ns) laser pulses, with good energy and temporal stability. High beam quality and stability were needed at the same time. These requirements are naturally connected to each other: the request of short pulses translates in a condition on the cavity length which in turn affects the maximum spot size of the sustained fundamental transverse mode and eventually the maximum energy we can extract from the MO. A shorter cavity is preferred for intrinsic minor sensitivity to thermal lens effects. On the other hand a longer radius of curvature (ROC) gives rise to higher diffraction losses, but it produces a larger beam diameter along the cavity length. All this considered, we tested our quasi-semi-confocal resonator with two different cavity lengths and with two output coupler ROCs (both OCs had a partially reflecting dielectric coating with $R = 80\%$ at 1.064 µm). The pump pulse duration was fixed at 200 µs and the optimum Q-switch delay was derived from output power measurements and set at 210 µs. In Table 1 we report pulse durations and output energies corresponding to different cavity configurations. Energy was measured using a calibrated Ophir power meter positioned at the laser output plane with a low-pass filter with cut-off wavelength at 850 nm to reject any signal coming from the pump beam.

Results show that using the shorter cavity length (100 mm) and pump power higher than 65% we can obtain pulses between 6 and 8 ns, with energy between 0.7 and 1 mJ. Correspondingly we obtain a nearly TEM_{00} output beam with a 99% diameter around 0.9 mm at the output coupler. Details of the beam properties are given in the following paragraph. Pulse shapes are shown in Fig. 1, acquired by a Newport 818-BB-31 InGaAs photodetector with rise time < 225 ps, for three different pump power levels. They give evidence of an expected pulse compression for higher values of the pump power, together with the appearance of some signal modulation over the pulse shape, due to the beatings of longitudinal modes. The pulse fast Fourier transform in Fig. 2 (taken for cavity length of 150 mm and 60% pump power) shows two secondary peaks at 820 and 1660 MHz consistent with a FSR of 821 MHz calculated with a cavity optical path length of 182.4 mm. The temporal results are in accordance with theoretical calculations [2], from which we can derive the pulse duration as a function of the initial inversion ratio, cavity round trip losses and cavity length as follows

$$\tau_{\text{P}} = \frac{r\eta}{r - 1 - \ln r} T_{\text{c}} = \frac{r\eta}{r - 1 - \ln r} \frac{2L}{c} \cdot \frac{1}{\Gamma}\,, \tag{1}$$

where r is the initial inversion ratio (growing with the pumping energy) and η is a parameter defining the energy extraction efficiency. A reduction approximately of 30% of the pulse

OC ROC (mm)	Cavity length (mm)	MO pump power (%)	Pulse duration (ns)	Output energy (mJ)
500	150	40	17.8	0.4
500	150	60	11.6	0.8
500	150	70	10.4	1.0
500	100	40	11.0	0.4
500	100	60	8.0	0.9
500	100	70	6.2	1.0
700	100	55	10.0	0.3
700	100	65	7.5	0.5
700	100	75	6.8	0.7

TABLE 1 Master oscillator pulse duration and output energy in different resonator configurations

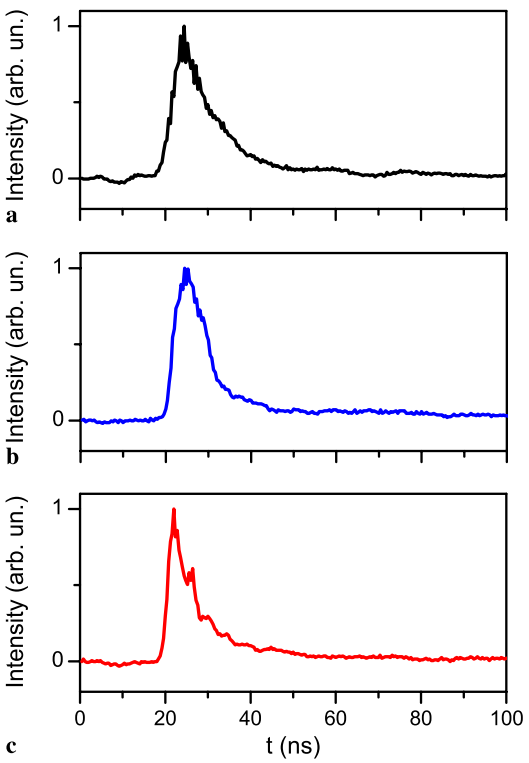

FIGURE 1 Pulse shape in the case of resonator length $L = 100$ mm and output coupler ROC = 700 mm for different pump current levels: (**a**) 55%, (**b**) 65% and (**c**) 75%

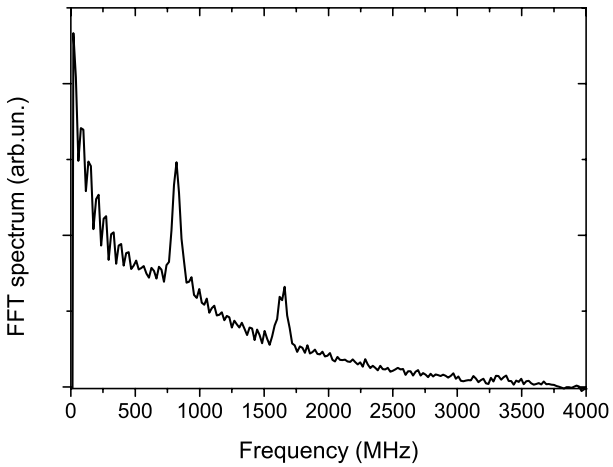

FIGURE 2 Pulse FFT in the case of resonator length $L = 150$ mm and output coupler ROC = 500 mm for pump current level of 60%

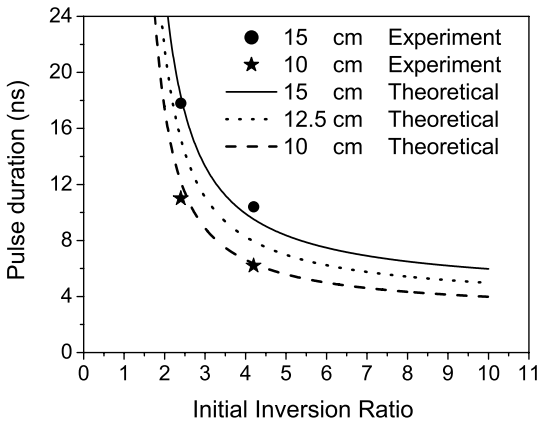

FIGURE 3 Theoretical calculations of the pulse duration for cavity length $L = 100$, 125, 150 mm and cavity round trip losses = 20% vs. initial inversion ratio (extraction efficiency $\eta = 0.8$)

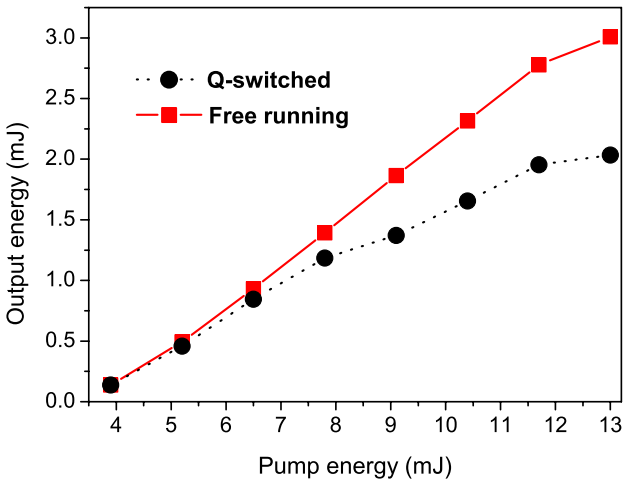

FIGURE 4 Measured master oscillator output energy vs. incident pump energy level. Cavity length $L = 150$ mm and output mirror ROC = 500 mm

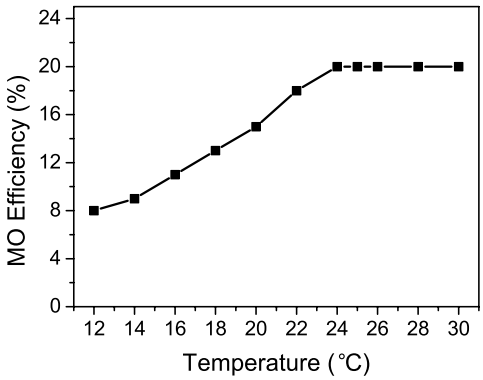

FIGURE 5 Master oscillator extraction efficiency as a function of the laser diode bar temperature. The current level is set to 50%

length with the reduction of the cavity length from 150 to 100 mm is foreseen, as well as the reduction with the increase of the pump power level. A comparison of our experimental results with the expected pulse durations is shown in Fig. 3.

Figure 4 shows the measured MO output energy at 1.064 μm vs. the incident pump energy in the case of 150 mm long resonator cavity and 500 mm ROC output coupler. A maximum Q-switched output energy of 2 mJ was obtained at a 100% pump level (corresponding to an incident energy of 13 mJ). The resulting optical conversion efficiency is 15%, and it peaks to 22% operating in Free-running (non-Q-switched) mode. We verified that the O–O efficiency was maintained within a ±5% range over a temperature interval of 12 °C. In Fig. 5 the oscillator efficiency is reported as a function of the laser diode bar temperature and for supply current level set to 50%.

2.3 *MO laser beam quality*

A high beam quality is one of the most important requirements for our source, as it determines the final divergence of the high energy beam to be used in the altitude measurements. To characterize the quality of our MO beam we performed a knife edge measurement following the ISO standard procedure [3]. To do this we produced a secondary waist using a 1.5″ diameter, 700 mm e.f.l. lens. The lens was placed 1175 mm far from the laser output plane, where the diameter of the circle containing 99% of the beam power was of the order of 6 mm (thus much smaller than the lens aperture). We then set up a knife-edge beam measuring system capable of analyzing the beam intensity distribution over a propagation distance longer than four Rayleigh ranges ($z_R = \pi w_f^2/\lambda$, approximately 25 cm) and containing the secondary beam waist. This fulfils the request of measuring the beam in the near and far field simultaneously. An Ophir LaserStar Power meter equipped with an 3A-P-SH (s/n 134051) measuring head was placed at the end of this path, beyond the measuring knife-edge stop. The beam size is obtained measuring the rise (fall) time between two clipping levels and multiplying it by the knife edge moving speed. Then beam diameters are calculated using the suitable correction coefficients [4] and the value of the propagation parameter M^2 is obtained from fitting of experimental caustic curves as detailed in [4]. The M_σ^2 value defined by the second order moments is then calculated from the M_{ke}^2 value obtained with the previously described knife-edge method using the following equation [3]:

$$\sqrt{M_\sigma^2} = 0.81\left(\sqrt{M_{ke}^2} - 1\right) + 1\,. \tag{2}$$

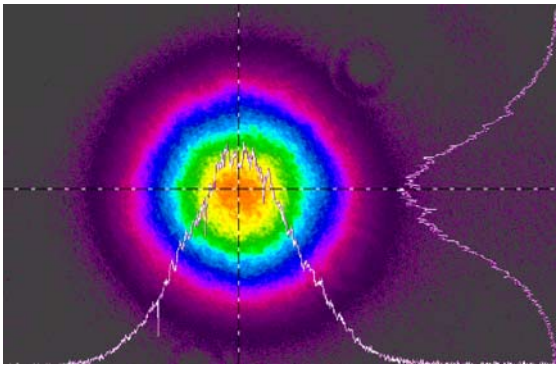

FIGURE 6 Beam intensity distribution in the far field acquired by LBA-FW-SCOR20 CCD camera

The diameters were measured in both horizontal and vertical directions using a Dove prism to perform a rotation of 90° of the beam before the focusing lens. We also investigated the beam intensity distributions in the far field, collecting the beam by a CCD-based beam analyzer (Spiricon LBA-FW-SCOR20). Figure 6 shows the beam intensity distribution acquired by the CCD camera in a plane approximately 45 cm far from the laser output.

The measured beam diameters for the two resonator cavity configurations that gave the best laser performance in terms of pulse duration and energy (ROC = 500 mm/L = 100 mm and ROC = 700 mm/L = 100 mm, see Table 1) are shown in Figs. 7 and 8. The M^2 values have been measured using two different clipping levels (10%–90% and 16%–84% [3]). Then they have been corrected using (2) and therefore the values given in legend must be read as second order moments-M^2.

3 Preliminary power amplifier performance

3.1 *PA design*

The goal of this work is that of obtaining a compact, possibly single-stage, high-gain power amplifier (PA) with a large tolerance to temperature variations. With this target we designed and investigated a multi-pass slab-shaped power amplifier. In our first prototypes the slab has Brewster angle and uncoated front faces, in order to avoid possible damage to AR coatings typical of high energy pulse operations. This slab shape produces a zigzag propagation in the slab narrow cross-section direction, based on total internal reflection (TIR). TIRs are guaranteed by a SiO_2 protective coating. The slab is passively cooled by metallic holders in thermal contact with the large TIR faces. The MO beam enters the slab on one side of the front face larger dimension and is then multiply reflected by two folding mirrors in such a way as to fill most of the slab volume. The optical scheme of the overall master-oscillator-multi-pass amplifier is shown in Fig. 9.

In this scheme the beam passes the amplifier forth and back five times before exiting the folding mirrors system. It eventually re-enters the system to repeat the entire path towards the oscillator. The returning beam is spatially separated from the beam entering the amplifier by a small tilt of the end mirror and a suitable external propagation path. This means that the amplifying beam makes ten trips in the amplifier (with a gain region length of the order of 20 mm). Such a short gain length enables a high pumping density and reduces losses due to ASE effects. Regarding the final beam pointing stability it can be easily demonstrated that any tilt of the folding mirrors

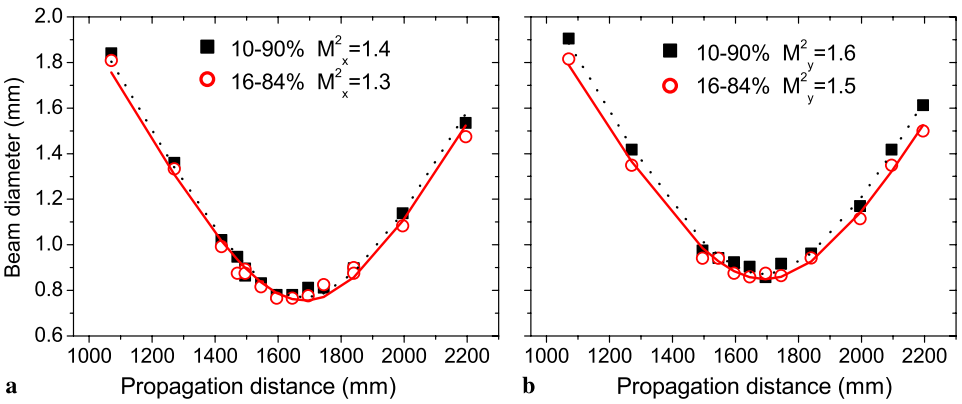

FIGURE 7 Beam diameter measurements in the horizontal (**a**) and vertical (**b**) direction obtained with the following resonator configuration: output coupler ROC = 500 mm and cavity length L = 100 mm

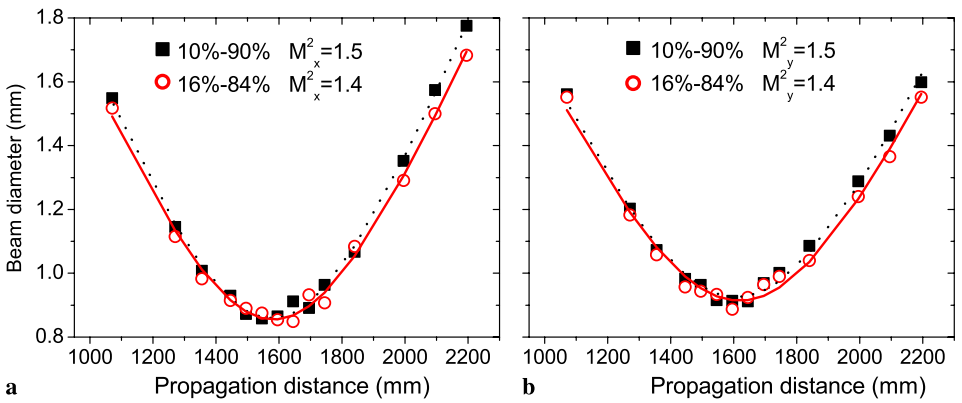

FIGURE 8 Beam diameter measurements in the horizontal (**a**) and vertical (**b**) direction obtained with the following resonator configuration: output coupler ROC = 700 mm and cavity length L = 100 mm

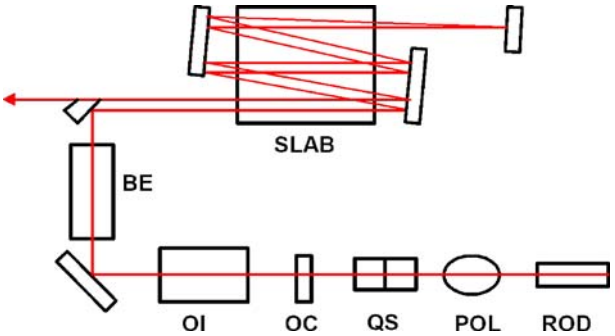

FIGURE 9 Optical scheme of the overall MOPA system. ROD: MO active medium; POL: polarizer; QS: Q-switch; OC: MO output coupler; OI: optical isolator; BE: beam expander; SLAB: PA active medium

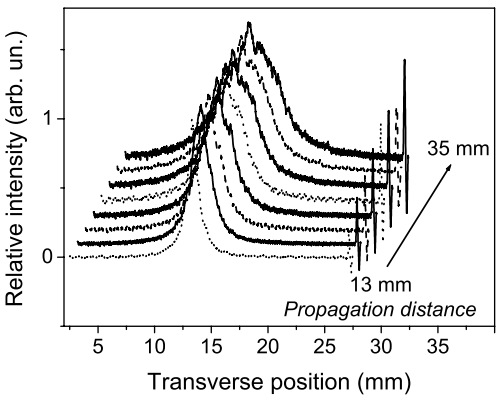

FIGURE 10 Spatial profile of the diode stack emission in the vertical (FA) direction

system results not affecting the final beam axis, provided that the two mirrors are solidly bound to each other.

The slabs used in our first set of experiments were 20 mm wide and had lateral dimensions of 37.8×4 mm^2. We tested three different samples with the same geometry: two ceramic YAG slabs with 0.6 and 1% Nd doping, and one crystal slab with a 1% Nd doping. The crystal produced higher propagation losses compared to the ceramic samples, that could be due either to depolarization of the incident beam and consequent loss on the Brewster faces or, more probably, to lower quality internal reflections. The slabs have been pumped on each lateral face by two diode bar arrays. Each array consists in 5 fast-axis (FA) collimated bars and is capable of a 500 W maximum emission during the Qcw on-cycles.

The four diode arrays are set 17 mm far from the slab lateral faces and their radiation is only partially collimated. Figure 10 shows a single diode-stack emission FA profile measured by means of a SPIRICON LASER PROBE 256-11 linear array of pyro-electric detectors. Evaluating the diode stack divergence in terms of encircled energy, we found that 80% of the power is contained in a 8° half-angle cone. As a consequence of this and of further possible misalignments between the four arrays, we expect not more than 70% of the power emitted by the four diode-bar stacks to enter the slab faces and effectively pump the amplifier volume. Thus, no more than 1400 W of pump power are to be considered in the amplifier efficiency characterization.

The small signal gain of the amplifier can be inferred using typical Nd:YAG amplifier system data reported by Koechner [5], assuming 200 μs-pump pulses at 808 nm, with 1400 W total pump power. Considering a fluorescence lifetime of 230 μs, as reported in the literature for 1% Nd-doped YAG, the expected small-signal gain g_0 is in the range 0.3–0.4 cm^{-1} and should produce single-pass gains up to 2. The saturation energy has been calculated considering a beam spot diameter of 4 mm and a saturation energy density of 200 mJ/cm^2. This enables us to estimate a saturation energy of 24 mJ. The output energy will be of course a function of the overlap of the different beam passages with the gain distribution inside the slab amplifier. The final mode-to-gain overlap is rather hard to model depending on the different multipass-cell tilt angles. In spite of that we can estimate two limiting cases in which each trip (five passages) in the amplifier fill 90% of the slab and are totally overlapped (no tilt in the external mirror) or totally separated (ideal tilt of the final mirror). These two limiting estimations predict an extraction efficiency for the multi-pass amplifier between 18 and 32%.

3.2 *Preliminary single-pass and multi-pass gain characterization*

The gain performance of our slab amplifier scheme has been tested using a commercial Quantel-ULTRA Nd:YAG laser as pulse generator, providing 8 ns pulses at up to 3 mJ energy level (after beam expansion and filtering). In the preliminary characterization measurements reported in this section, for a simpler interpretation of the amplifier mechanisms we removed the folding mirror. Therefore the seeded beam makes five zigzag passages in the pumped slab. Because of the large number of parameters involved in the amplifier overall performances, we limit our analysis to the property most important for our application, namely the temperature behaviour of the multi-pass amplifier. Single and multipass gain characterisation runs have been performed on all the samples. Maximization of gain has involved, for every measurement set, both the evaluation of optimal PA pump pulse length (as the energy storage capability of the active medium is connected to the $^4F_{3/2}$ state lifetime, which depends on the doping level and sample quality) and the assessment of optimal delay between PA pump pulse and MO pulse. The gain performances of the single-crystalline slab were similar to those obtained for the ceramic sample with the same 1%-Nd doping level, sug-

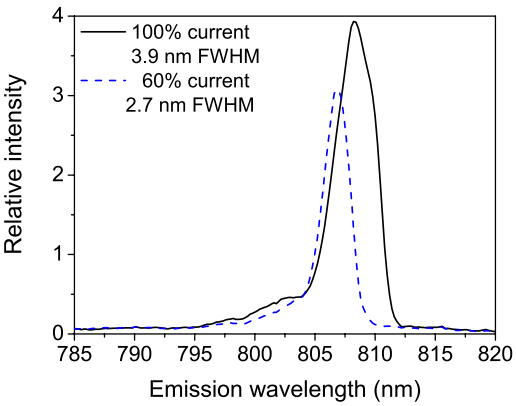

FIGURE 11 Emission spectra of the PA pump stacks at different current levels

gesting that thermally induced depolarization losses [6] are negligible in our Brewster-cut slab setup. To better understand the thermal behaviour of our PA we have to take into account the diode emission spectra (peak wavelength and lineshape). The radiation emitted by the four diode stacks pumping our PA has been characterized by means of an Avantis Avaspec fiber spectrometer having 0.3 nm resolution. Figure 11 shows the emitted spectra for 60 and 100% current level operation, collected at a distance where the radiation lobes of (at least two) stacks are overlapped. A significant line broadening is evidenced at higher currents, possibly due to unequal cooling of the different bars or stacks.

These spectral properties result extremely important, as the fraction F of pump power absorbed at a depth x is given by the expression:

$$F(x,T) = \frac{\int_{\lambda_{\min}}^{\lambda_{\mathrm{MAX}}} I(\lambda,T)\mathrm{e}^{-\alpha(\lambda)x}\,\mathrm{d}\lambda}{\int_{\lambda_{\min}}^{\lambda_{\mathrm{MAX}}} I(\lambda,T)\,\mathrm{d}\lambda}, \tag{3}$$

were $\alpha(\lambda)$ is the absorption spectrum of the Nd:YAG and $I(\lambda, T)$ is the spectral distribution of the emitted intensity from the pumping arrays. We acquired the absorption spectra of our Nd:YAG samples by means of a dual-beam Perkin–Elmer "Lambda 900" spectrophotometer (resolution 0.5 nm) and we calculated the fraction of absorbed power using (3) for several different cases of diode radiation and Nd dopings.

Figures 12 and 13 show the different calculated behaviours of 0.3, 0.6 and 1%-doped slabs when pumped with the radiation spectrum (1.3 nm FWHM) of a single cw stack and with the radiation spectrum (3.9 nm FWHM) of our Qcw diode bars arrays. It is clearly seen that the total absorbed pumping power for a given doping level is sensibly different. In other words the optimal doping level turns out to be strictly related to the pump array spectral properties.

From the above calculated absorbed pump power, a higher doping level results preferable in terms of efficiency optimization. It has to be considered though that doping level and pump radiation spectrum also affect the distribution of absorbed pump radiation inside the slab. This distribution is given by the expression:

$$A(x,T) = \frac{\int_{\lambda_{\min}}^{\lambda_{\mathrm{MAX}}} I(\lambda,T)\alpha(\lambda)\mathrm{e}^{-\alpha(\lambda)x}\,\mathrm{d}\lambda}{\int_{\lambda_{\min}}^{\lambda_{\mathrm{MAX}}} I(\lambda,T)\,\mathrm{d}\lambda}. \tag{4}$$

Plots of the calculated absorbed power distributions are reported in Fig. 14 for a 1.3 nm-wide pump spectrum, and in Fig. 15 for a 3.9 nm-wide pump spectrum. Distributions refer to a two sided pumped slab as the one of our experiments.

It is now clear that a lower doping and a broader spectrum enable the inversion of the central part of the slab as well, and thus the generation of an useful gain in the entire cross-

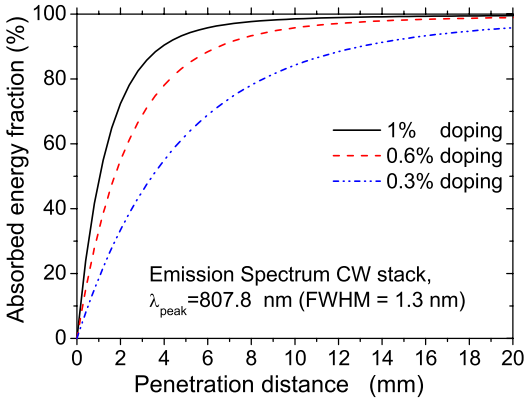

FIGURE 12 Calculated absorbed pump power fraction in the case of a narrow (1.3 nm FWHM) emission spectrum

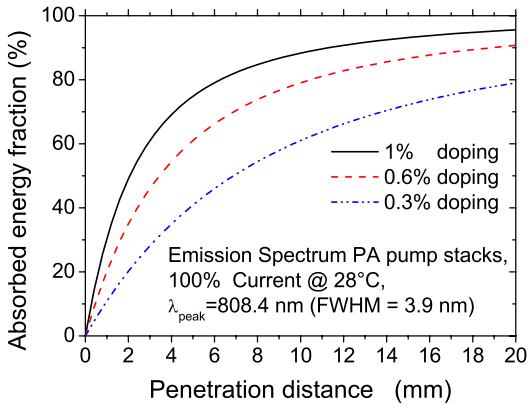

FIGURE 13 Calculated absorbed pump power fraction in the case of a broader (3.9 nm FWHM) emission spectrum

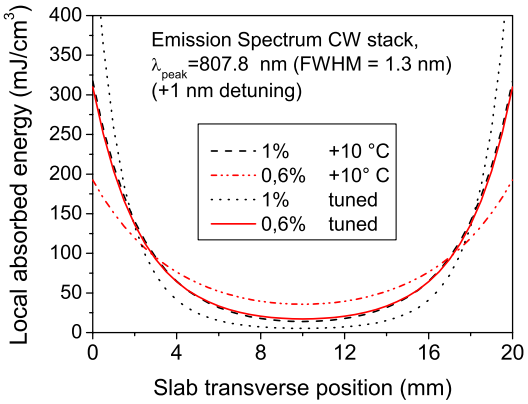

FIGURE 14 Calculated pump power distributions in the case of a narrow (1.3 nm FWHM) emission spectrum

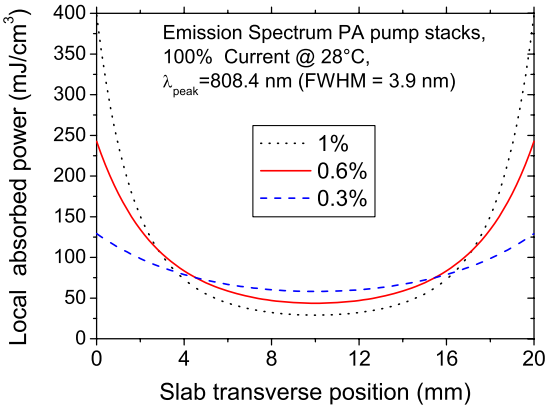

FIGURE 15 Calculated pump power distributions in the case of a broader (3.9 nm FWHM) emission spectrum

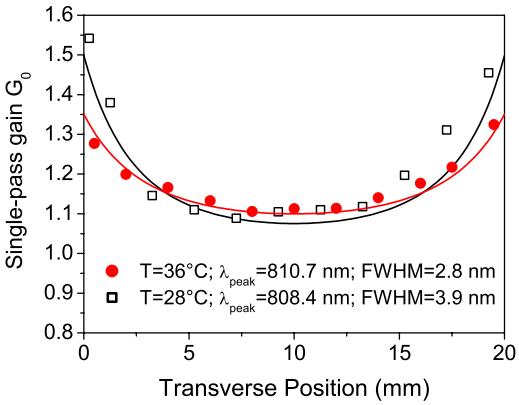

FIGURE 16 Measured and calculated single-pass gain distributions. Diode spectra adopted in calculations are those measured in the real operating conditions

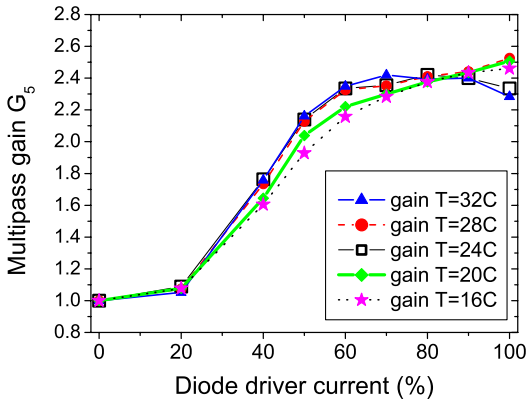

FIGURE 17 Measured multi-pass gain curves for different current and diode temperature conditions, for the 0.6% Nd:YAG slab

section of the slab amplifier. A reasonable trade-off must be made between efficient pumping and uniform gain distribution. Following [5] we can relate the small signal gain g_0 to the pump energy density as:

$$g_0 = \beta E_{\mathrm{st}}\,, \tag{5}$$

where β is a constant characteristic of the gain medium and its value is 4.73 cm^2/J for Nd:YAG [5], while E_{st} is the energy density stored in the amplifier. It can be related to the pump energy density E_{pump} by the following relation:

$$E_{\mathrm{st}} = \eta_{\mathrm{s}}\eta_{\mathrm{q}}\eta_{\mathrm{B}}\eta_{\mathrm{ASE}}\eta_{\mathrm{st}}\eta_{\mathrm{co}}E_{\mathrm{pump}}\,, \tag{6}$$

where: $\eta_{\mathrm{s}} = 0.76$ is the Nd Stokes shift; η_{q} is the quantum efficiency (extremely high in case of a well tuned pump diode); η_{B} is the pumped volume to beam overlap efficiency; η_{ASE} is the gain reduction due to amplified spontaneous emission; η_{st} is the storing efficiency (0.67 for 1% doping, 0.69 for 0.6% doping); η_{co} is the pump radiation coupling efficiency (about 0.7 in our present scheme).

Assuming the product to have a maximum value around 0.73 for the optimized system (with a pumping quantum efficiency as uniform as possible) we end with (6) having a global efficiency product equal to 0.28. Figure 16 shows two sets of single pass gain values obtained for different pumping conditions from the 0.6% doping slab. The measurements are compared to theoretical estimations made in the previous discussion and fitted with a global efficiency half the optimal value (0.28) previously estimated. The good agreement of the experimental data to the curves validates the modelling approach and indicates that further optimization is needed in the tunable parameters (η_{q}, η_{B}, η_{co} and possibly η_{ASE}) to reach a higher gain level. Figure 17 reports the experimental 5-pass gain (G_5) measurements performed on the same slab for different pumping diodes temperatures. The curves are consistent with the single pass gain distributions and remain close to each other in an interval as wide as 16 °C.

3.3 *Power amplifier optimization*

As discussed in the previous two sections the power amplifier is still in a preliminary stage of its development. The pumping system is still to be thoroughly characterized and optimized. The 70% coupling from diode stacks to slab is estimated from the single stack characterization. Possible misalignments of the four stacks further reduce this efficiency factor. The multi-pass folding cavity has mirror mountings that do not yet allow a perfect alignment. Indeed the side peaked distribution of the stored energy requests a total filling of the slab width by the travelling beam to be amplified. A better cavity with sharp-edge mirrors is presently under investigation. Table 2 reports the expected single pass and five-pass gains obtained from our modelling. Multi-pass gain values are given with a minimum and maximum value corresponding to present and optimized alignment. Bold values are those corresponding to the results experimentally obtained so far.

Considering that the path folding step (from 5 to 10 passages) gives a squared value for the final unsaturated gain, our target for the five passages gain is around a value of seven.

4 Conclusions

We have reported on the design and development of activities carried on in our facilities towards the construction

Slab doping	G_0 50% η		G_0 70% η		G_0 100% η		G_5 50% η		G_5 70% η		G_5 100% η	
	Center	Side	Center	Side	Center	Side	min	MAX	min	MAX	min	MAX
0.3%	1.21	1.35	1.30	1.53	1.47	1.84	2.9	3.7	4.4	6.2	8.7	14.1
0.6%	**1.14**	**1.57**	1.19	1.89	1.30	2.46	**2.4**	4.5	3.1	7.9	5.6	20.0
1.0%	**1.07**	**1.70**	1.09	2.07	1.14	2.87	**1.7**	4.4	2.1	7.6	3.0	19.0

TABLE 2 Measured and expected single-pass and multi-pass gain values. η is the overall efficiency

of an extremely compact diode-pumped Q-switched Nd:YAG source for space applications. The MO activities are complete while the PA amplifier is still in an early stage of development. This latter device, having a new scheme, has been thoroughly characterized and modelled. Improving steps have been defined and are presently in progress. Calculations enable us to foresee a 25–50 mJ output with the required characteristics both from the viewpoint of temporal and propagation behaviours.

ACKNOWLEDGEMENTS This work has been performed within the ESA contract No. 19368/NL/IA. We thank Alberto Cosentino, Alessia Mondello, Luciano Calamai, Marco Barilli, Antonio Padelli, Fausto Rosadi, Massimo Malenotti, Michele Felet and Emilio Nocentini (Selex Galileo) and Massimo D'Uva, Mauro Pucci (INOA-CNR) for collaboration.

REFERENCES

1 A.E. Siegman, *Lasers* (University Science Books, Mill Valley, CA, 1986), pp. 746–747
2 W. Koechner, *Solid-State Laser Engineering*, 5th. rev. edn. (Springer, Berlin, 1999), pp. 469–473
3 See the ISO standards 11146-1, Lasers and laser-related equipment-test methods for laser beam widths, divergence angle and beam propagation factor – Part 1: stigmatic and simple astigmatic beams and 11146-3 Lasers and laser-related equipment-test methods for laser beam widths, divergence angle and beam propagation factor – Part 3: Alternative test methods and geometrical laser beam classification and propagation
4 M. Ciofini, E. Favilla, A. Lapucci, E. Sani, Opt. Laser Technol. **39**, 1380 (2007)
5 W. Koechner, *Solid-State Laser Engineering*, 5th. rev. edn. (Springer, Berlin, 1999), pp. 152–176
6 M. Ostermeyer, D. Mudge, P.J. Veitch, J. Munch, Appl. Opt. **45**, 5368 (2006)